



Age of Jupiter inferred from the distinct genetics and formation times of meteorites

Thomas S. Kruijer^{a,b,1}, Christoph Burkhardt^a, Gerrit Budde^a, and Thorsten Kleine^a

^aInstitut für Planetologie, University of Münster, 48149 Muenster, Germany; and ^bNuclear and Chemical Sciences Division, Lawrence Livermore National Laboratory, Livermore, CA 94550

Edited by Neta A. Bahcall, Princeton University, Princeton, NJ, and approved May 4, 2017 (received for review March 23, 2017)

The age of Jupiter, the largest planet in our Solar System, is still unknown. Gas-giant planet formation likely involved the growth of large solid cores, followed by the accumulation of gas onto these cores. Thus, the gas-giant cores must have formed before dissipation of the solar nebula, which likely occurred within less than 10 My after Solar System formation. Although such rapid accretion of the gas-giant cores has successfully been modeled, until now it has not been possible to date their formation. Here, using molybdenum and tungsten isotope measurements on iron meteorites, we demonstrate that meteorites derive from two genetically distinct nebular reservoirs that coexisted and remained spatially separated between ~1 My and ~3–4 My after Solar System formation. The most plausible mechanism for this efficient separation is the formation of Jupiter, opening a gap in the disk and preventing the exchange of material between the two reservoirs. As such, our results indicate that Jupiter's core grew to ~20 Earth masses within <1 My, followed by a more protracted growth to ~50 Earth masses until at least ~3–4 My after Solar System formation. Thus, Jupiter is the oldest planet of the Solar System, and its solid core formed well before the solar nebula gas dissipated, consistent with the core accretion model for giant planet formation.

Jupiter | giant planet formation | nucleosynthetic isotope anomalies | Hf-W chronometry | solar nebula

The formation of gas-giant planets such as Jupiter and Saturn is thought to have involved the growth of large solid cores of ~10–20 Earth masses (M_E), followed by the accumulation of gas onto these cores (1, 2). Thus, the gas-giant cores must have formed before dissipation of the solar nebula—the gaseous circumstellar disk surrounding the young Sun—which likely occurred between 1 My and 10 My after Solar System formation (3). Although such rapid accretion of the gas-giant cores has successfully been modeled (1, 2, 4), until now it has not been possible to actually date their formation. Here we show that the growth of Jupiter can be dated using the distinct genetic heritage and formation times of meteorites.

Most meteorites derive from small bodies located in the main asteroid belt between Mars and Jupiter. Originally these bodies probably formed at a much wider range of heliocentric distances, as suggested by the distinct chemical and isotopic compositions of meteorites (5–8) and by dynamical models indicating that the gravitational influence of the gas giants led to scattering of small bodies into the asteroid belt (9, 10). Information on the initial formation location of meteorite parent bodies within the solar accretion disk can be obtained from nucleosynthetic isotope anomalies in meteorites. These anomalies arise through the heterogeneous distribution of isotopically anomalous presolar components and vary as a function of heliocentric distance (6, 11). For instance, Cr, Ti, and Mo isotope anomalies (6–8, 12) reveal a fundamental dichotomy in the genetic heritage of meteorites, distinguishing between “noncarbonaceous” and “carbonaceous” meteorite reservoirs (11). This distinction may reflect either a temporal change in disk composition or the separation of materials accreted inside [noncarbonaceous (NC) meteorites] and outside [carbonaceous (CC) meteorites] the orbit of Jupiter (11–14). If the

latter is correct, then the age of Jupiter can be determined by assessing the formation time and longevity of the NC and CC meteorite reservoirs. However, it is currently not known when these two reservoirs formed and whether and for how long they remained isolated from each other.

To address these issues and to ultimately determine the timescale of Jupiter's formation, we obtained W and Mo isotopic data for iron meteorites (*Materials and Methods, SI Materials and Methods, Fig. S1, and Tables S1–S4*). These samples are fragments of the metallic cores from some of the earliest-formed planetesimals (15), making them ideal samples to search for the effects of giant planet formation on the dynamics of the early Solar System. Previous W isotope studies on iron meteorites have focused on the major groups (i.e., IIAB, IID, IIIAB, IVA, and IVB) and on determining the timescales and processes of core formation in these bodies (15). Here we extend these studies by examining a larger set of iron meteorite groups (i.e., IC, IIC, IID, IIF, IIIE, and IIIF), for which we determined the timing of core formation using the ¹⁸²Hf–¹⁸²W chronometer (half-life = 8.9 My), as well as nucleosynthetic Mo isotopic signatures, which enables us to link these irons to either the NC or the CC meteorites.

CC and NC Iron Meteorites

The Mo isotopic data reveal variable nucleosynthetic anomalies in iron meteorites (Fig. 1). Consistent with prior studies (6), we find that these anomalies predominantly reflect the heterogeneous distribution of a presolar carrier enriched in Mo nuclides produced in the slow neutron capture process (*s*-process) of nucleosynthesis (Fig. 1). However, in a plot of $\epsilon^{95}\text{Mo}$ vs. $\epsilon^{94}\text{Mo}$ (the parts per 10,000 deviations of ⁹⁵Mo/⁹⁶Mo and ⁹⁴Mo/⁹⁶Mo from terrestrial standard values), the iron meteorites fall onto

Significance

Jupiter is the most massive planet of the Solar System and its presence had an immense effect on the dynamics of the solar accretion disk. Knowing the age of Jupiter, therefore, is key for understanding how the Solar System evolved toward its present-day architecture. However, although models predict that Jupiter formed relatively early, until now, its formation has never been dated. Here we show through isotope analyses of meteorites that Jupiter's solid core formed within only ~1 My after the start of Solar System history, making it the oldest planet. Through its rapid formation, Jupiter acted as an effective barrier against inward transport of material across the disk, potentially explaining why our Solar System lacks any super-Earths.

Author contributions: T.S.K. and T.K. designed research; T.S.K. and C.B. performed research; T.S.K., C.B., G.B., and T.K. analyzed data; and T.S.K., C.B., G.B., and T.K. wrote the paper.

The authors declare no conflict of interest.

This article is a PNAS Direct Submission.

¹To whom correspondence should be addressed. Email: thomaskruijer@gmail.com.

This article contains supporting information online at www.pnas.org/lookup/suppl/doi:10.1073/pnas.1704461114/-DCSupplemental.

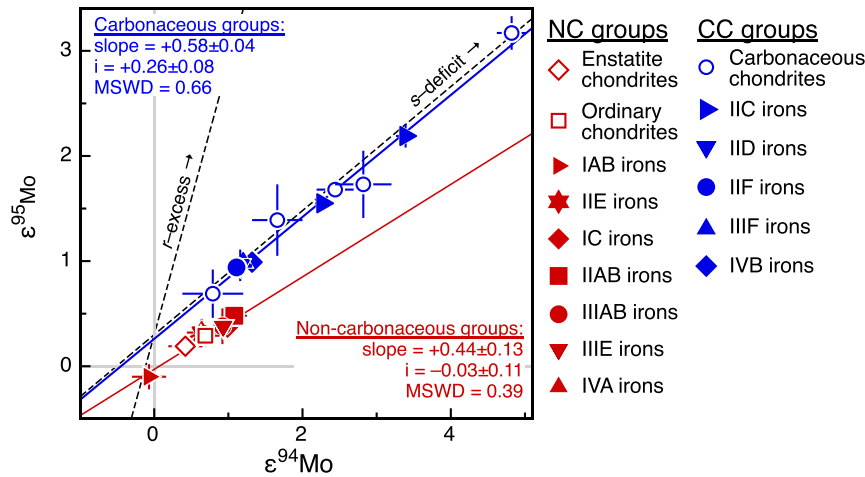


Fig. 1. Molybdenum isotope dichotomy of iron meteorite groups. Iron meteorites and chondrites define two distinct trends in $\epsilon^{95}\text{Mo}$ vs. $\epsilon^{94}\text{Mo}$ space, separating a CC (blue symbols) from a NC reservoir (red symbols). Note that the two regressions (solid lines) through the iron meteorite and chondrites from NC and CC reservoirs yield significantly different $\epsilon^{95}\text{Mo}$ intercept values. Error bars denote 95% conf. limits on group mean values. Also shown are s -process and r -process mixing lines (dashed lines), plotted at an ordinate $\epsilon^{95}\text{Mo}$ of $+0.3$ and calculated using the Mo isotopic composition of presolar SiC grains (37), representing s -process Mo and the corresponding r -process residuals. Note that other Mo isotopes show consistent systematics (Fig. S5). Data for IC, IIC, IID, IIF, IIIIF, and IIIIE iron meteorites are from this study and data for chondrites and other iron meteorite groups are from ref. 6.

two distinct s -process mixing lines. Whereas most of the newly investigated irons (IIC, IID, IIF, and IIIIF) plot on an s -process mixing line together with carbonaceous chondrites, most of the previously studied irons as well as the IC and IIIIE irons plot on another s -process mixing line together with ordinary chondrites, enstatite chondrites, and the Earth's mantle ($\epsilon^1\text{Mo} = 0$) (Fig. 1). Thus, several iron meteorite groups (IIC, IID, IIF, IIIIF, and IVB) belong to the CC meteorites, whereas several other groups (IC, IIAB, IIIAB, IIIIE, and IVA) belong to the NC meteorites (Fig. 1).

A similar genetic dichotomy is seen for W isotopes, which for iron meteorites reveal two distinct clusters of $\epsilon^{182}\text{W}$ and $\epsilon^{183}\text{W}$ (the parts per 10,000 deviations of $^{182}\text{W}/^{184}\text{W}$ and $^{183}\text{W}/^{184}\text{W}$ from terrestrial standard values). The NC irons have $\epsilon^{182}\text{W}$ values between approximately -3.4 and -3.3 and no nucleosynthetic W isotope anomalies (i.e., $\epsilon^{183}\text{W} \sim 0$), whereas the CC irons have $\epsilon^{182}\text{W}$ values of around -3.2 and show nucleosynthetic $\epsilon^{183}\text{W}$ excesses (Fig. 2, Fig. S2, and Table S5). Note that the $\epsilon^{182}\text{W}$ values of each group were corrected for the effects of cosmic ray exposure (Figs. S3 and S4 and Table S5), using Pt isotopes as the neutron dosimeter (15). In addition, for the iron groups showing ^{183}W anomalies, the $\epsilon^{182}\text{W}$ values were corrected for nucleosynthetic $\epsilon^{182}\text{W}$ variations, by using correlated $\epsilon^{182}\text{W}-\epsilon^{183}\text{W}$ variations induced by nucleosynthetic isotope heterogeneities (15) (see SI Text for details).

As variable $\epsilon^{182}\text{W}$ values in iron meteorites reflect different times of Hf/W fractionation during metal-silicate separation on their parent bodies (15–17), the higher $\epsilon^{182}\text{W}$ of the CC irons indicates a later time of core formation (Table S5), at ~ 2.2 My to ~ 2.8 My, compared with the NC irons, at ~ 0.3 My to ~ 1.8 My after the start of Solar System history [as defined by the formation of Ca-Al-rich inclusions (CAI)]. A prior study has shown that $\epsilon^{182}\text{W}$ differences between different groups of iron meteorites could be due to distinct melting temperatures during core formation, reflecting the different S contents and hence liquidus temperatures of the cores (15). However, the NC and CC reservoirs both include iron meteorite groups with similar volatile element concentrations and, hence, presumably similar S contents. Thus, different melting temperatures of the NC and CC parent bodies cannot be the cause of the observed $\epsilon^{182}\text{W}$ dichotomy. Instead, the difference in core formation times is most easily explained by different accretion times of the CC and NC iron meteorite

parent bodies. Thermal modeling of bodies internally heated by ^{26}Al decay (SI Text) shows that the NC iron meteorite parent bodies probably accreted within <0.4 My after CAI formation, whereas the CC iron meteorite parent bodies accreted slightly later, at $0.9^{+0.4}_{-0.2}$ My after CAI formation (Fig. 3). Taken together, the Mo and W isotopic data thus indicate that accretion of CC and NC iron meteorite parent bodies occurred not only in genetically distinct nebular regions, but also at different times (Figs. 2 and 3).

Coexistence and Spatial Separation of CC and NC Meteorite Reservoirs

The distinct genetic heritage and accretion times of iron meteorite parent bodies make it possible to constrain the formation time and longevity of the NC and CC nebular reservoirs. Accretion of CC iron meteorite parent bodies at ~ 1 My after CAI formation

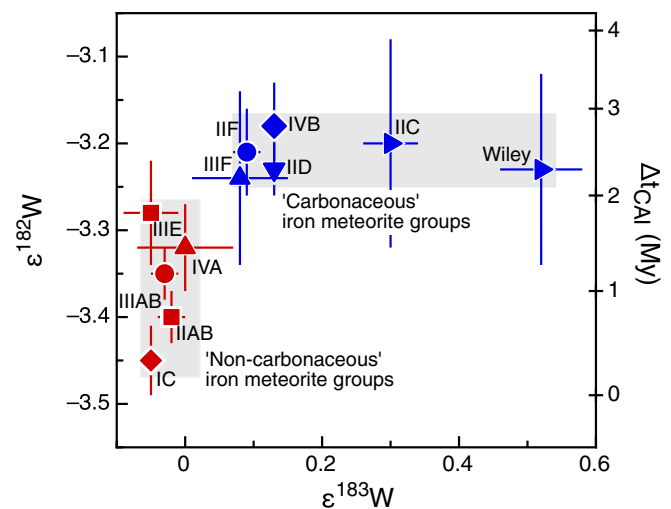


Fig. 2. Tungsten isotope dichotomy of iron meteorite groups. Error bars denote 95% conf. intervals on group mean values. $\epsilon^{182}\text{W}$ signatures were corrected for effects of nucleosynthetic heterogeneity and secondary neutron capture (SI Text). Plotted on the right ordinate axis are two-stage Hf-W model ages of core formation (see SI Text for details). See Fig. 1 for symbol legend.

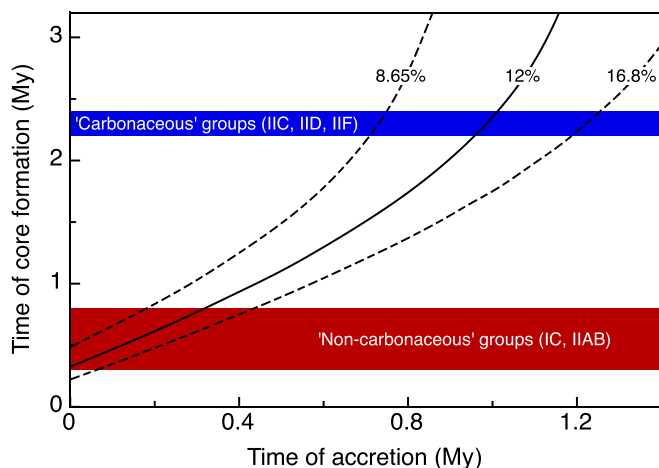


Fig. 3. Relation between the time of accretion and core formation on iron meteorite parent bodies. Curves show thermal modeling results quantifying the relation between the time of core formation and the time of parent body accretion (*SI Text*), for different Al concentrations of the bulk parent bodies (for 8.65 wt%, 12 wt%, and 16.8 wt% Al). Colored areas show the observed core formation ages of NC iron meteorite parent bodies and CC parent bodies.

implies that by this time, the NC and CC reservoirs were already separated. The distinction between the NC and CC reservoirs most likely reflects the addition of presolar material enriched in r -process nuclides to the solar nebula region from which the CC meteorites derive (12). Given that all CC meteorites plot on a single s -process mixing line with a constant offset compared with the NC line (Fig. 1), they all have the same r -process excess relative to the NC meteorites. Consequently, this r -process component must have been added to and homogeneously distributed within the CC reservoir before the first CC bodies formed. The ^{182}W data for the CC irons, therefore, indicate that this addition of material and, hence, the formation of the CC reservoir occurred within ~ 1 My of Solar System formation.

A key constraint from our results is that the accretion of ordinary chondrite parent bodies in the NC reservoir (i.e., at ~ 2 My) (18) occurred after the accretion of iron meteorite parent bodies in the CC reservoir (at ~ 1 My). Thus, the existence of the NC and CC reservoirs cannot simply reflect a compositional change of the solar nebula over time. Instead, the CC and NC nebular reservoirs must have existed contemporaneously and remained spatially separated within the solar circumstellar disk. The timespan over which this separation persisted can be inferred by considering the accretion times of the youngest meteorite parent bodies in each reservoir. This is because in the $\epsilon^{95}\text{Mo}-\epsilon^{94}\text{Mo}$ diagram (Fig. 1), no meteorites plot between the CC and NC lines, meaning that the NC and CC reservoirs cannot have mixed but instead must have remained isolated from each other until parent body accretion in the NC and CC reservoirs terminated. As accretion of chondrite parent bodies occurred at ~ 2 My after CAI formation in the NC reservoir (ordinary chondrites) and until $\sim 3-4$ My in the CC reservoir (CC chondrites) (18–20), this means that the NC and CC reservoirs must have remained isolated from each other from <1 My until at least $\sim 3-4$ My after CAI formation. This prolonged spatial separation of the NC and CC reservoirs cannot simply reflect a large distance between these reservoirs within the disk, because the rapid speed of grain drift in the disk would have facilitated efficient mixing on much shorter timescales (21, 22). One way to avoid the inward drift of material would be the rapid accumulation of these grains into planetesimals. However, this also cannot explain the efficient separation of the NC and CC

reservoirs, because in both reservoirs planetesimal accretion occurred concurrently for several million years. Consequently, the precursor dust of planetesimals in both reservoirs must have been present for this period and, therefore, cannot have been locked up in earlier-formed planetesimals.

The most plausible mechanism to efficiently separate two disk reservoirs for an extended period is the accretion of a giant planet in between them, generating a gap within the disk and inhibiting the inward drift of dust grains (13, 23, 24) (Fig. 4). Being the largest and nearest gas-giant planet, Jupiter is the most likely candidate for separating the NC and CC reservoirs. As the Earth is part of the NC reservoir, this implies that the CC reservoir was initially located outside Jupiter's orbit, meaning that CC bodies originally derive from the outer Solar System. Because the CC meteorites include some iron meteorites, one important implication of our data is that early and rapid formation of differentiated planetesimals was possible not only in the innermost terrestrial planet region (25), but also farther out in the disk.

The formation of Jupiter between the NC and CC reservoirs not only provides a mechanism for efficiently separating these two reservoirs for an extended period, but also provides a means for the later transport of CC bodies into the inner Solar System. This is necessary because although the NC and CC bodies initially formed in spatially distinct areas of the disk, at the present day they both reside in the main asteroid belt. This is a natural outcome of the growth of Jupiter, which ultimately leads to scattering of bodies from beyond Jupiter's orbit (i.e., CC bodies) into the inner Solar System, either during an inward-then-outward migration of Jupiter (10, 23) or during runaway growth of Jupiter on a fixed orbit (26). Thus, the presence of Jupiter between the NC and CC reservoirs provides the most plausible mechanism to

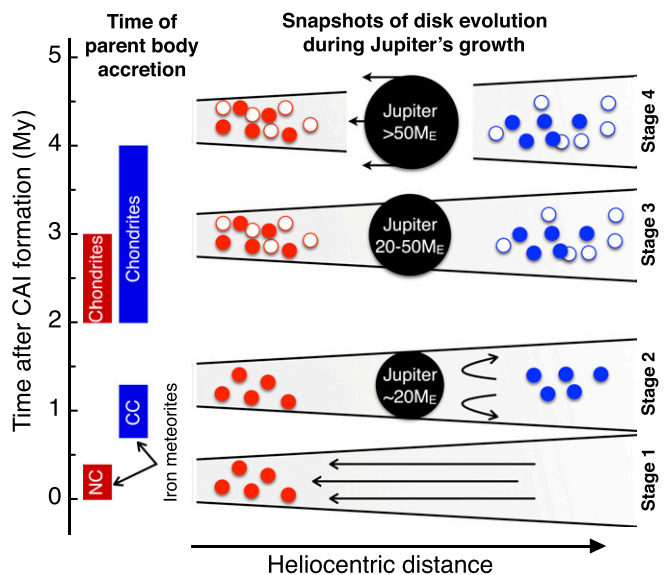


Fig. 4. Four snapshots of Jupiter's growth in the solar circumstellar disk. At stage 1, within <0.4 My after CAI, the NC iron meteorite parent bodies (red solid symbols) accreted in a continuous gas disk characterized by inward drag of solids. At stage 2, around ~ 1 My after CAI, iron meteorite parent bodies of the CC reservoir (blue solid symbols) had accreted and Jupiter had already grown to $\sim 20 M_E$, preventing any inward drag of solids (24). At stage 3, from ~ 2 My to ~ 4 My after CAI, Jupiter grew further through gas accretion onto its core. Moreover, the ordinary chondrite parent bodies (red open symbols) accreted in the NC reservoir and CC chondrite parent bodies (blue open symbols) accreted in the CC reservoir. At stage 4, after $\sim 3-4$ My after CAI, Jupiter had grown to $\sim 50 M_E$ and had opened a gap in the disk (13, 23, 24), likely resulting in the inward migration of Jupiter. Solid boxes (*Left*) show the accretion ages of iron meteorite and chondrite parent bodies in the NC and CC reservoirs (see *CC and NC Iron Meteorites*).

account for both (i) the prolonged spatial separation of these reservoirs and (ii) the co-occurrence of NC and CC bodies in the present-day asteroid belt.

Growth History of Jupiter

With the assumption that the prolonged spatial separation of the NC and CC reservoirs reflects the formation of Jupiter in between these reservoirs, the distinct timescales for the accretion of NC and CC meteorite parent bodies make it possible to date the formation of Jupiter. The growth of Jupiter beyond a certain mass would have inhibited the inward drift of particles (13, 24), and once it grew further, Jupiter ultimately would have generated a gap within the disk (23). In particular, theoretical studies suggest that the inward drift of particles stopped once Jupiter's core had grown to about $20 M_E$ (24), while a gap formed once Jupiter reached approximately $50 M_E$ (13, 23, 27). Thus, because the r -process material that was added to the CC reservoir did not infiltrate the coexisting yet spatially separated NC reservoir, this implies that at the time the r -process material was added, Jupiter already had a size of $>20 M_E$. Furthermore, because this material must have been added and homogenized before the first planetesimals formed within the CC reservoir at ~ 1 My after CAI formation, these results mandate that Jupiter reached a size of $>20 M_E$ within ~ 1 My of Solar System formation (Fig. 4). This early formation of (proto-) Jupiter is consistent with the rapid growth of Jupiter's core predicted in theoretical models (1, 4), regardless of whether pebble accretion (28, 29) or hierarchical growth models (30, 31) are assumed.

Once Jupiter reached a mass of $50 M_E$, which happens via gas accretion onto its solid core, a gap opened in the disk (13, 23, 24, 27), followed by scattering of bodies from beyond Jupiter's orbit (i.e., CC bodies) into the inner Solar System (10, 23, 26). Our results show that this scattering of CC bodies and, hence, Jupiter's outward migration or runaway growth cannot have started before ~ 3 – 4 My after CAI formation. This is because CC chondrite parent bodies continued to form until at least ~ 3 – 4 My after CAI formation (18–20). As these chondrites plot on the CC line in Mo isotope space (Fig. 1), they must have formed before the scattering of CC meteorites into the inner Solar System and, hence, before the CC meteorite parent bodies joined the NC parent bodies in the asteroid belt. Accordingly, these data indicate that Jupiter reached $\sim 50 M_E$ later than ~ 3 – 4 My after CAI formation. This is consistent with theoretical predictions that the rapid growth of Jupiter's core to $\sim 20 M_E$ was followed by

a more protracted stage of gas and solid accretion to several tens of Earth's masses (1, 32, 33) before runaway gas accretion led to Jupiter's final mass ($\sim 318 M_E$). Thus, our results are in good agreement with the timing and sequence of events predicted in the core accretion model for the formation of Jupiter (1). One important implication of this result is that, because Jupiter acted as a barrier against inward transport of solids across the disk, the inner Solar System remained relatively mass deficient, possibly explaining its lack of any "super-Earths" (34, 35).

Materials and Methods

For this study we selected a total of 19 samples covering six different rare iron meteorite groups (IC, IIC, IID, IIF, IIIE, and IIIF). This sample set complements the iron meteorites from major groups (IIAB, IID, IIIAB, IVA, and IVB) whose W, Pt, and Mo isotope compositions had previously been analyzed (6, 15). After digestion of the iron meteorites in concentrated HNO_3 -HCl (2:1), the sample solutions were split into a fraction for W and Mo ($\sim 90\%$) and for Pt ($\sim 10\%$) isotope analysis. The chemical separation of W, Pt, and Mo was accomplished using ion exchange chromatography following previously published procedures (6, 12, 15, 36). The W, Pt, and Mo isotope compositions were measured on a ThermoScientific Neptune Plus MC-ICPMS in the Institut für Planetologie at the University of Münster (12, 15, 36) (see *SI Materials and Methods* for details). Instrumental mass bias was corrected by internally normalizing to $^{186}\text{W}/^{184}\text{W} = 0.92767$, $^{198}\text{Pt}/^{195}\text{Pt} = 0.2145$, and $^{98}\text{Mo}/^{96}\text{Mo} = 1.453173$, using the exponential law. The W, Pt, and Mo isotope data are reported as ϵ -unit (i.e., parts per 10^4) deviation relative to the isotopic ratios measured for terrestrial bracketing solution standards. The reported $\epsilon^i\text{W}$, $\epsilon^i\text{Pt}$, and $\epsilon^i\text{Mo}$ values for samples (Tables S1–S4) represent the mean of pooled solution replicates ($n = 1$ – 8) together with their associated uncertainties [2 SD or 95% confidence (conf.) interval].

ACKNOWLEDGMENTS. We gratefully acknowledge the Natural History Museum, London (C. Smith, N. Almeida) and the Field Museum, Chicago (P. Heck) for providing samples. We thank F. Nimmo for giving detailed insights into giant planet formation and for a first draft of Fig. 4. We also thank G. Brenneka and A. Morbidelli for discussions; C. Brenneka for comments on the paper; and S. Gerber, J. Hellmann, N. Krabbe, and U. Heitmann for their assistance. Finally, we thank Alex Halliday and two anonymous reviewers for their constructive comments that helped to improve the paper. This study was performed under the auspices of the US DOE by Lawrence Livermore National Laboratory under Contract DE-AC52-07NA27344 with release number LLNL-JRNL-731226. This work was funded by the Deutsche Forschungsgemeinschaft (DFG) Collaborative Research Center/Transregio TRR 170 subproject B3-1). C.B. was supported by the European Research Council Consolidator grant ISOCORE (Contract 616564), and G.B. was supported by the DFG Priority Program 1385 (Grant KL1857/3). This is TRR 170 publication 10.

- Pollack JB, et al. (1996) Formation of the giant planets by concurrent accretion of solids and gas. *Icarus* 124:62–85.
- Mizuno H, Nakazawa K, Hayashi C (1978) Instability of a gaseous envelope surrounding a planetary core and formation of giant planets. *Prog Theor Phys* 60:699–710.
- Haisch KE, Lada EA, Lada CJ (2001) Disk frequencies and lifetimes in young clusters. *Astrophys J* 553:L153–L156.
- Helled R, et al. (2014) *Giant Planet Formation, Evolution, and Internal Structure. Protostars and Planets VI* (Univ of Arizona Press, Tucson, AZ).
- Dauphas N, Schauble EA (2016) Mass fractionation laws, mass-independent effects, and isotopic anomalies. *Annu Rev Earth Planet Sci* 44:709–783.
- Burkhardt C, et al. (2011) Molybdenum isotope anomalies in meteorites: Constraints on solar nebula evolution and origin of the Earth. *Earth Planet Sci Lett* 312:390–400.
- Trinquier A, Birck J, Allegre CJ (2007) Widespread ^{54}Cr heterogeneity in the inner solar system. *Astrophys J* 655:1179–1185.
- Trinquier A, et al. (2009) Origin of nucleosynthetic isotope heterogeneity in the solar protoplanetary disk. *Science* 324:374–376.
- Levison HF, et al. (2009) Contamination of the asteroid belt by primordial trans-Neptunian objects. *Nature* 460:364–366.
- Walsh KJ, Morbidelli A, Raymond SN, O'Brien DP, Mandell AM (2011) A low mass for Mars from Jupiter's early gas-driven migration. *Nature* 475:206–209.
- Warren P (2011) Stable-isotopic anomalies and the accretionary assemblage of the Earth and Mars: A subordinate role for carbonaceous chondrites. *Earth Planet Sci Lett* 311:93–100.
- Budde G, et al. (2016) Molybdenum isotopic evidence for the origin of chondrules and a distinct genetic heritage of carbonaceous and non-carbonaceous meteorites. *Earth Planet Sci Lett* 454:293–303.
- Morbidelli A, et al. (2016) Fossilized condensation lines in the Solar System protoplanetary disk. *Icarus* 267:368–376.
- Van Kooten EMM, et al. (2016) Isotopic evidence for primordial molecular cloud material in metal-rich carbonaceous chondrites. *Proc Natl Acad Sci USA* 113:2011–2016.
- Kruijer TS, et al. (2014) Protracted core formation and rapid accretion of protoplanets. *Science* 344:1150–1154.
- Qin L, Dauphas N, Wadhwa M, Masarik J, Janney PE (2008) Rapid accretion and differentiation of iron meteorite parent bodies inferred from ^{182}Hf - ^{182}W chronometry and thermal modeling. *Earth Planet Sci Lett* 273:94–104.
- Kleine T, Mezger K, Palme H, Scherer E, Münker C (2005) Early core formation in asteroids and late accretion of chondrite parent bodies: Evidence from ^{182}Hf - ^{182}W in CAIs, metal-rich chondrites, and iron meteorites. *Geochim Cosmochim Acta* 69:5805–5818.
- Kita NT, Ushikubo T (2012) Evolution of protoplanetary disk inferred from ^{26}Al chronology of individual chondrules. *Meteorit Planet Sci* 47:1108–1119.
- Connelly JN, et al. (2012) The absolute chronology and thermal processing of solids in the solar protoplanetary disk. *Science* 338:651–655.
- Schrader DL, et al. (2016) Distribution of ^{26}Al in the CR chondrite chondrule-forming region of the protoplanetary disk. *Geochim Cosmochim Acta* 201:275–302.
- Weidenschilling SJ (1977) Aerodynamics of solid bodies in the solar nebula. *Mon Not R Astron Soc vol* 180:57–70.
- Birnstiel T, Dullemond CP, Pinilla P (2013) Lopsided dust rings in transition disks. *Astron Astrophys* 550:L8.
- Lin DNC, Papaloizou J (1986) On the tidal interaction between protoplanets and the protoplanetary disk. III - Orbital migration of protoplanets. *Astrophys J* 309:846.
- Lambrechts M, Johansen A, Morbidelli A (2014) Separating gas-giant and ice-giant planets by halting pebble accretion. *Astron Astrophys* 572:A35.
- Botke WF, Nesvorny D, Grimm RE, Morbidelli A, O'Brien DP (2006) Iron meteorites as remnants of planetesimals formed in the terrestrial planet region. *Nature* 439:821–824.
- Kretke KA, Levison HF, Bottke W (2016) Exploring how giant planet formation affected the asteroid belt. *Proceedings of the 48th Meeting of the Division for Planetary Sciences* (Am Astron Soc, Washington, DC), abstract 25.

27. Crida A, Morbidelli A, Masset F (2006) On the width and shape of gaps in protoplanetary disks. *Icarus* 181:587–604.
28. Lambrechts M, Johansen A (2012) Rapid growth of gas-giant cores by pebble accretion. *Astron Astrophys* 544:A32.
29. Levison HF, Kretke KA, Duncan MJ (2015) Growing the gas-giant planets by the gradual accumulation of pebbles. *Nature* 524:322–324.
30. Kokubo E, et al. (2002) Formation of protoplanet systems and diversity of planetary systems. *Astrophys J* 581:666–680.
31. Desch SJ, et al. (2007) Mass distribution and planet formation in the solar nebula. *Astrophys J* 671:878–893.
32. Monga N, Desch S (2014) External photoevaporation of the solar nebula: Jupiter's noble gas enrichments. *Astrophys J* 798:9.
33. Johnson BC, Walsh KJ, Minton DA, Krot AN, Levison HF (2016) Timing of the formation and migration of giant planets as constrained by CB chondrites. *Sci Adv* 2: e1601658.
34. Izidoro A, Raymond SN, Morbidelli A, Hersant F, Pierens A (2015) Gas giant planets as dynamical barriers to inward-migrating super-Earths. *Astrophys J* 800:L22.
35. Morbidelli A, Raymond SN (2016) Challenges in planet formation. *J Geophys Res* 121: 1962–1980.
36. Kruijjer TS, et al. (2013) Neutron capture on Pt isotopes in iron meteorites and the Hf–W chronology of core formation in planetesimals. *Earth Planet Sci Lett* 361:162–172.
37. Nicolussi GK, et al. (1998) Molybdenum isotopic composition of individual presolar silicon carbide grains from the Murchison meteorite. *Geochim Cosmochim Acta* 62: 1093–1104.
38. Prombo CA, Clayton RN (1993) Nitrogen isotopic compositions of iron meteorites. *Geochim Cosmochim Acta* 57:3749–3761.
39. Marty B, Chaussidon M, Wiens RC, Jurewicz AJ, Burnett DS (2011) A ^{15}N -poor isotopic composition for the solar system as shown by Genesis solar wind samples. *Science* 332: 1533–1536.
40. Rehkämper M, Halliday ANN (1997) Development and application of new ion-exchange techniques for the separation of the platinum group and other siderophile elements from geological samples. *Talanta* 44:663–672.
41. Kruijjer TS, et al. (2012) Hf–W chronometry of core formation in planetesimals inferred from weakly irradiated iron meteorites. *Geochim Cosmochim Acta* 99:287–304.
42. Willbold M, Elliott T, Moorbath S (2011) The tungsten isotopic composition of the Earth's mantle before the terminal bombardment. *Nature* 477:195–198.
43. Budde G, Kruijjer TS, Fischer-Gödde M, Kleine T (2015) Planetary differentiation revealed by the Hf–W systematics of ureilites. *Earth Planet Sci Lett* 430:316–325.
44. Kruijjer TS, Kleine T, Fischer-Gödde M, Burkhardt C, Wieler R (2014) Nucleosynthetic W isotope anomalies and the Hf–W chronometry of Ca–Al-rich inclusions. *Earth Planet Sci Lett* 403:317–327.
45. Kruijjer TS, Kleine T, Fischer-Gödde M, Sprung P (2015) Lunar tungsten isotopic evidence for the late veneer. *Nature* 520:534–537.
46. Cook DL, Kruijjer TS, Leya I, Kleine T (2014) Cosmogenic ^{180}W variations in meteorites and re-assessment of a possible ^{184}Os – ^{180}W decay system. *Geochim Cosmochim Acta* 140:160–176.
47. Cook DL, Schönbächler M (2016) High-precision measurement of W isotopes in Fe–Ni alloy and the effects from the nuclear field shift. *J Anal At Spectrom* 31:1400–1405.
48. Masarik J (1997) Contribution of neutron-capture reactions to observed tungsten isotopic ratios. *Earth Planet Sci Lett* 152:181–185.
49. Leya I, Wieler R, Halliday AN (2003) The influence of cosmic-ray production on extinct nuclide systems. *Geochim Cosmochim Acta* 67:529–541.
50. Budde G, Kleine T, Kruijjer TS, Burkhardt C, Metzler K (2016) Tungsten isotopic constraints on the age and origin of chondrules. *Proc Natl Acad Sci USA* 113:2886–2891.
51. Burkhardt C, Kleine T, Dauphas N, Wieler R (2012) Nucleosynthetic tungsten isotope anomalies in acid leachates of the Murchison chondrite: Implications for hafnium-tungsten chronometry. *Astrophys J* 753:L6.
52. Qin L, et al. (2008) Tungsten nuclear anomalies in planetesimal cores. *Astrophys J* 674: 1234–1241.
53. Wittig N, Humayun M, Brandon D, Huang S, Leya I (2013) Coupled W–Os–Pt isotope systematics in IVB iron meteorites: In situ neutron dosimetry for W isotope chronology. *Earth Planet Sci Lett* 361:152–161.
54. Burkhardt C, Schönbächler M (2015) Intrinsic W nucleosynthetic isotope variations in carbonaceous chondrites: Implications for W nucleosynthesis and nebular vs. parent body processing of presolar materials. *Geochim Cosmochim Acta* 165:361–375.
55. Walker RJ (2012) Evidence for homogeneous distribution of osmium in the protosolar nebula. *Earth Planet Sci Lett* 351–352:36–44.
56. Qin L, Dauphas N, Horan MF, Leya I, Carlson RW (2015) Correlated cosmogenic W and Os isotopic variations in Carbo and implications for Hf–W chronology. *Geochim Cosmochim Acta* 153:91–104.
57. Kleine T, et al. (2009) Hf–W chronology of the accretion and early evolution of asteroids and terrestrial planets. *Geochim Cosmochim Acta* 73:5150–5188.
58. Vockenhuber C, et al. (2004) New half-life measurement of ^{182}Hf : Improved chronometer for the early solar system. *Phys Rev Lett* 93:172501.
59. Neumann W, Breuer D, Spohn T (2012) Differentiation and core formation in accreting planetesimals. *Astron Astrophys* 543:A141.
60. Hevey PJ, Sanders IS (2006) A model for planetesimal meltdown by ^{26}Al and its implications for meteorite parent bodies. *Meteorit Planet Sci* 41:95–106.
61. Norris TL, Gancarz AJ, Roico DJ, Thomas KW (1983) Half-life of ^{26}Al . *Proc 14th Lunar Planet Sci Conf* 88:331–333.
62. Lodders K, Fegley B (1998) *The Planetary Scientist's Companion* (Oxford Univ Press, New York).
63. Taylor GJ (1992) Core formation in asteroids. *J Geophys Res* 97:14717.
64. McCoy TJ, Mittlefehldt DW, Wilson L (2006) Asteroid differentiation. *Meteorites and the Early Solar System II*, eds Lauretta DS, McSween HYJ (Univ of Arizona Press, Tucson, AZ), pp 733–745.

Supporting Information

Kruijer et al. 10.1073/pnas.1704461114

SI Materials and Methods

Samples and Chemical Separation of W, Pt, and Mo. For this study we selected 16 samples covering five different rare iron meteorite groups (IC, IIC, IIF, IIIE, and IIIF; Tables S2–S4). We targeted these samples because some of them (e.g., IIC iron meteorites) show ^{15}N signatures suggestive of an outer Solar System origin (38, 39). These iron meteorite samples, therefore, are prime candidates for differentiated bodies that might have accreted beyond Jupiter. In addition, we also analyzed 3 IID iron meteorites that complement the Pt–W isotope dataset for IID iron meteorites obtained previously (36). Samples (~ 0.2 – 1.5 g) were cut using a diamond saw, polished with abrasives (SiC), and ultrasonically cleaned in ethanol to remove any saw marks and adhering dust. To remove any terrestrial contamination, the samples were then mildly leached in 6 M HCl (plus trace HNO_3) on a hotplate at $\sim 90^\circ\text{C}$ for ~ 10 min. The iron meteorites were digested in 20 mL concentrated HNO_3 –HCl (2:1) on a hotplate at 130°C for at least 24 h. Upon complete digestion the sample solutions were split into a fraction for W and Mo ($\sim 90\%$) and for Pt ($\sim 10\%$) isotope analysis.

The chemical separation of Pt followed previously published procedures (36) and is based on the techniques initially described in ref. 40. Tungsten and Mo were sequentially separated from the sample matrix using anion exchange chromatography (4 mL Biorad AG1X8, 200–400 mesh) (41), where W was eluted using 15 mL 6 M HCl–1 M HF, followed by Mo using 10 mL 3 M HNO_3 . The W cuts from the first column were further purified using a cleanup anion chromatography step, which essentially is a miniaturized version of the first column with only 1 mL resin (41). To obtain Mo cuts with sufficiently low Ru/Mo and Zr/Mo, the Mo cuts from the first column were further purified using two additional ion chromatography steps, using Eichrom TRU resin (6). Total yields after the chemical separation were ~ 70 – 100% for W, $\sim 70\%$ for Pt, and $\sim 70\%$ for Mo. Total procedural blanks were < 200 pg for W, < 100 pg for Pt, and $< 1,000$ pg for Mo. These blank amounts are inconsequential because of the large amount of each element analyzed (~ 250 ng W, ~ 100 – 400 ng Pt, and ~ 500 – 800 ng Mo).

Mass Spectrometry. The W, Pt, and Mo isotope compositions were measured on a ThermoScientific Neptune Plus MC-ICPMS in the Institut für Planetologie at the University of Münster. The analytical methods for high-precision W, Pt, and Mo isotope analyses were largely based on previously reported procedures (12, 15, 36). Samples and standards for W, Pt, and Mo isotope measurements were introduced into the mass spectrometer, using ESI or Teledyne Cetac C-flow self-aspirating PFA nebulizers (~ 50 – 60 $\mu\text{L}/\text{min}$) connected to a Teledyne Cetac Aridus II desolvator system. For W, the measurements were performed in low-resolution mode, using Jet sampler and X-skimmer cones. All four major W isotopes (^{182}W , ^{183}W , ^{184}W , and ^{186}W) were measured simultaneously. Total ion beams of ~ 2 – 3×10^{10} were obtained for ~ 30 -ppb W standard solutions at an uptake rate of ~ 60 $\mu\text{L}/\text{min}$. Electronic baselines were obtained before each sample measurement by deflecting the beam using the electrostatic analyzer for 60 s and then subtracted from sample signal intensities. A single W isotope measurement comprised 200 cycles of 4.2 s integration time each. Small isobaric interferences from ^{184}Os and ^{186}Os on W isotope ratios were corrected by monitoring interference-free ^{188}Os and were generally much smaller than ~ 5 ppm on $^{182}\text{W}/^{184}\text{W}$. Instrumental mass bias was corrected by internal normalization to either $^{186}\text{W}/^{183}\text{W} = 1.9859$ (denoted “6/3”) or $^{186}\text{W}/^{184}\text{W} = 0.92767$ (denoted “6/4”), using the exponential law.

The W isotope analyses of samples were bracketed by measurements of terrestrial solution standards (Alfa Aesar; batch 22312), whose concentrations matched those of the sample solutions to within ~ 10 – 20% .

For Pt, the measurements were performed in low-resolution mode, using standard Ni sampler and (H) skimmer cones. Total ion beams of ~ 2 – 4×10^{10} were obtained for ~ 200 -ppb Pt standard solutions at uptake rates of ~ 50 – 60 $\mu\text{L}/\text{min}$. Five Pt isotopes (^{192}Pt , ^{194}Pt , ^{195}Pt , ^{196}Pt , and ^{198}Pt) were measured simultaneously, and each measurement comprised a 60-s electronic baseline measurement followed by 100 isotope ratio measurements of 4.2 s integration time each. Instrumental mass bias was corrected by internally normalizing to either $^{196}\text{Pt}/^{195}\text{Pt} = 0.7464$ (denoted “6/5”) or $^{198}\text{Pt}/^{195}\text{Pt} = 0.2145$ (denoted “8/5”), using the exponential law. All Pt isotope data are reported in ϵ^{Pt} , as the parts per 10^4 deviation in $^{196}\text{Pt}/^{195}\text{Pt}$ relative to the terrestrial bracketing solution standard analyses.

The Mo isotope compositions of iron meteorites were performed in low-resolution mode, using standard Ni sampler and (H) skimmer cones. Total ion beams of $\sim 1.1 \times 10^{10}$ were obtained for ~ 100 -ppb Mo standard solutions at an uptake rate of ~ 50 $\mu\text{L}/\text{min}$. Six Mo isotopes (^{92}Mo , ^{94}Mo , ^{95}Mo , ^{96}Mo , ^{98}Mo , and ^{100}Mo) were measured simultaneously, and each measurement consisted of 40 on-peak baseline measurements of 4.2 s each, followed by 100 isotope ratio measurements of 8.4 s integration time each. Although the measurement solutions generally had very low $^{91}\text{Zr}/^{96}\text{Mo}$ (< 0.00005) and $^{99}\text{Ru}/^{96}\text{Mo}$ (< 0.00001), potential isobaric interferences from remaining Zr and Ru were corrected for by monitoring interference-free ^{91}Zr and ^{99}Ru . The magnitude of these corrections was generally < 0.2 ϵ -units on ϵ^{Mo} . Only a few measurement solutions had larger Zr/Mo (i.e., up to $^{91}\text{Zr}/^{96}\text{Mo} \sim 0.002$ for Wiley), resulting in larger interference corrections (up to ~ 10 – 20 ϵ^{Mo} units). Nevertheless, measurements of Mo solution standards with admixed Zr and Ru demonstrate up to Zr inference corrections of ~ 25 ϵ on ϵ^{Mo} yield accurate results (12). Instrumental mass bias was corrected by internal normalization to $^{98}\text{Mo}/^{96}\text{Mo} = 1.453173$ (denoted “8/6”), using the exponential law. The W, Pt, and Mo isotope data are reported as ϵ -unit (i.e., parts per 10^4) deviation relative to the isotopic ratios measured for terrestrial bracketing solution standards. The reported ϵ^{W} , ϵ^{Pt} , and ϵ^{Mo} values for samples (Tables S2–S4) represent the mean of pooled solution replicates ($n = 1$ – 8) together with their associated external uncertainties.

Accuracy and Reproducibility of W, Pt, and Mo Isotope Measurements.

The accuracy and precision of the W, Pt, and Mo isotope measurements were assessed through analyses of terrestrial standards that were processed and analyzed alongside the iron meteorites (Tables S1 and S2 and Fig. S1). These analyses followed our well-established routines for high-precision W, Pt, and Mo measurements by MC-ICPMS (6, 12, 15, 36). Previous high-precision W isotope studies using MC-ICPMS observed very small excesses in $\epsilon^{182}\text{W}$ (6/3) and $\epsilon^{184}\text{W}$ (6/3) and corresponding deficits in $\epsilon^{183}\text{W}$ (6/4) for processed terrestrial standards, most likely caused by a nuclear field shift effect induced during incomplete redissolution of W in Savillex beakers (36, 41–47). The magnitude of the analytical ^{183}W effect varies among different studies and typically is between -0.1 and -0.2 $\epsilon^{183}\text{W}$ (41–43, 46). In the present study, we were able to minimize this effect by repeated dry downs of the samples with HClO_4 following each step of ion exchange separation of W. The repeated analyses of eight different digestions of the NIST129c metal standard processed

this way yielded a mean $\epsilon^{183}\text{W}$ of -0.03 ± 0.03 (95% conf. interval, $n = 8$, Table S1 and Fig. S2); the mean $\epsilon^{182}\text{W}$ (6/3) of the NIST129c analyses is $+0.05 \pm 0.03$ (95% conf. interval, $n = 8$), consistent with a small analytical ^{183}W effect for which we expect $\epsilon^{182}\text{W}$ (6/3) $\sim 1.5 \times \epsilon^{183}\text{W}$ (6/4). Thus, the average magnitude of this ^{183}W effect is significantly smaller than in previous studies and does not compromise the conclusions drawn from the $\epsilon^{183}\text{W}$ data. Finally, we underline that this analytical effect occurs only for normalizations involving ^{183}W . For this reason, the $\epsilon^{182}\text{W}$ (6/4) values—the normalization generally used for chronological interpretation—are not compromised by this effect.

SI Text

Quantifying Nucleosynthetic and Cosmogenic W Isotope Variations.

Determining the timescales of core formation in iron meteorite parent bodies using their ^{182}W compositions requires the prior quantification of any cosmogenic and nucleosynthetic ^{182}W variations in the investigated sample suite. Cosmogenic W isotope variations result from secondary neutron capture effects induced during cosmic ray exposure; these effects lead to downward shifts of $\epsilon^{182}\text{W}$ without affecting $\epsilon^{183}\text{W}$ (or $\epsilon^{184}\text{W}$) (17, 48, 49). Consequently, the correction for cosmogenic $\epsilon^{182}\text{W}$ effects requires the use of an independent in situ neutron dosimeter, such as Pt or Os isotopes (see below). Nucleosynthetic W isotope anomalies, on the other hand, arise from the heterogeneous distribution of *s*- and *r*-process components and result in correlated $\epsilon^{182}\text{W}$ – $\epsilon^{183}\text{W}$ (6/4) and $\epsilon^{182}\text{W}$ – $\epsilon^{184}\text{W}$ (6/3) variations (44, 50–52). Thus, the magnitude of nucleosynthetic $\epsilon^{182}\text{W}$ variations can be quantified using the $\epsilon^{183}\text{W}$ compositions determined for each group of irons (below). Note that variations in $\epsilon^{183}\text{W}$ (or $\epsilon^{184}\text{W}$) are solely of nucleosynthetic origin (neutron capture-induced variations of the $^{183}\text{W}/^{184}\text{W}$ ratio cancel out by mass bias correction to a fixed $^{186}\text{W}/^{184}\text{W}$ or $^{186}\text{W}/^{183}\text{W}$), and so a reliable correction for nucleosynthetic W isotope anomalies is possible even for strongly irradiated samples.

Nucleosynthetic W isotope anomalies. The iron meteorites analyzed in the present study show a significant range in their ^{183}W compositions with measured $\epsilon^{183}\text{W}$ values between about -0.14 and $+0.52$ (Table S3 and Fig. S2). This range is larger than the scatter observed for the $\epsilon^{183}\text{W}$ measurements of the terrestrial metal standard NIST129c, indicating that some of the meteorites have resolved $\epsilon^{183}\text{W}$ anomalies. In particular, the positive $\epsilon^{183}\text{W}$ observed for several samples cannot be caused by the analytical ^{183}W effect (above), which can only produce negative $\epsilon^{183}\text{W}$. The IC and IIIE iron meteorites exhibit similar scatter in $\epsilon^{183}\text{W}$ to the NIST129c standard (Fig. S2) and, when normalized to the mean $\epsilon^{183}\text{W}$ of the NIST129c analyses, have mean $\epsilon^{183}\text{W}$ values of -0.05 ± 0.02 (IC irons) and -0.05 ± 0.04 (IIIE irons). Thus, these two groups of irons do not show evidence for any significant nucleosynthetic $\epsilon^{183}\text{W}$ anomalies, in agreement with the absence of such anomalies in the IIAB, IIIAB, and IVA iron meteorite groups (15). In contrast, resolved $\epsilon^{183}\text{W}$ excesses relative to the terrestrial standards (Alfa Aesar; NIST129c) are observed for the IIC, IID, and IIF irons analyzed in the present study (Fig. S2). Similar $\epsilon^{183}\text{W}$ excesses have previously been reported for IVB ($+0.13 \pm 0.02$) and IID ($+0.12 \pm 0.02$) irons (note that the three IID irons analyzed here exhibit similar $\epsilon^{183}\text{W}$ excesses to those found previously) (36, 52, 53). The IIIIF irons probably also show a similar $\epsilon^{183}\text{W}$ excess, but this value is not resolved at present. Whereas the IID, IIF, and IVB (and possibly the IIIIF) irons all exhibit similar $\epsilon^{183}\text{W} \sim +0.12$, the IIC irons show the largest $\epsilon^{183}\text{W}$ excesses yet observed for iron meteorites. Whereas Kumerina and Ballinoo exhibit uniform $\epsilon^{183}\text{W}$ excesses of $+0.30 \pm 0.04$, Wiley shows a distinctly higher $\epsilon^{183}\text{W}$ of $+0.54 \pm 0.06$ (Fig. S2). The difference between these two values is larger than the scatter observed for the NIST129c analyses and thus indicates nucleosynthetic W isotope heterogeneity among different members of the IIC group. Therefore, Wiley probably derives

from a distinct parent body from that of Kumerina and Ballinoo. Taken together, the ^{183}W systematics reveal a dichotomy between iron meteorite groups showing a nucleosynthetic W isotope anomaly (IIC, IID, IIF, IIIIF, and IVB) and those lacking such a signature (IC, IIAB, IIIAB, IIIIE, and IVA).

The effect of nucleosynthetic W isotope heterogeneity on $\epsilon^{182}\text{W}$ can be quantified using the $\epsilon^{183}\text{W}$ of a sample and the empirically defined linear relations between nucleosynthetic $\epsilon^{182}\text{W}$ and $\epsilon^{183}\text{W}$ (or $\epsilon^{184}\text{W}$) variations (36, 41, 51). Using W isotope data for bulk CAI yields a $\epsilon^{182}\text{W}$ (6/4) vs. $\epsilon^{183}\text{W}$ (6/4) slope of $+1.41 \pm 0.05$ (95% conf. interval) for data internally normalized to $^{186}\text{W}/^{184}\text{W}$ and a shallower $\epsilon^{182}\text{W}$ (6/3) vs. $\epsilon^{184}\text{W}$ (6/3) slope of -0.11 ± 0.05 for $^{186}\text{W}/^{183}\text{W}$ normalized data (44). These slopes are in excellent agreement with those obtained for leachates of CC chondrites (51, 54). Based on nucleosynthetic W isotope anomalies in Allende chondrules and matrix, slightly different slopes of $\epsilon^{182}\text{W}$ (6/4) vs. $\epsilon^{183}\text{W}$ (6/4) = $+1.25 \pm 0.06$ and $\epsilon^{182}\text{W}$ (6/3) vs. $\epsilon^{184}\text{W}$ (6/3) = $+0.12 \pm 0.07$ were obtained (50). However, the $\epsilon^{183}\text{W}$ anomalies observed for the samples investigated in the present study are so small that these differences in slopes are inconsequential for the correction of measured $\epsilon^{182}\text{W}$ values. Here, we corrected the measured $\epsilon^{182}\text{W}$ values of the IIC, IID, IIF, and IIIIF meteorites, using the mean $\epsilon^{183}\text{W}$ for each group and the empirical $\epsilon^{182}\text{W}$ vs. $\epsilon^{183}\text{W}$ slopes obtained from the CAI data. This procedure yields downward corrections on $\epsilon^{182}\text{W}$ of ~ 0.2 – 0.7 for the $^{186}\text{W}/^{184}\text{W}$ -normalized data and of <0.04 $\epsilon^{182}\text{W}$ for the $^{186}\text{W}/^{183}\text{W}$ -normalized data. Using the slopes from ref. 50 instead results in corrected $\epsilon^{182}\text{W}$ values that are only ~ 0.01 – 0.07 ϵ -units higher, that is, essentially within uncertainty.

Neutron capture effects and preexposure $\epsilon^{182}\text{W}$. Recent studies have shown that corrections for secondary neutron capture-induced $\epsilon^{182}\text{W}$ variations are possible using Pt (15, 36, 53) and Os isotopes (53, 55) as in situ neutron dosimeters. Here we use the same approach as in refs. 15 and 36 and determine “preexposure” $\epsilon^{182}\text{W}$ values (i.e., $\epsilon^{182}\text{W}$ unaffected by neutron capture) for each group of iron meteorites from the intercepts of empirical neutron capture-induced $\epsilon^{182}\text{W}$ vs. $\epsilon^{196}\text{Pt}$ correlation lines. Using this method, the preexposure $\epsilon^{182}\text{W}$ values for the five major iron meteorite groups (IIAB, IID, IIIAB, IVA, and IVB) were determined in a previous study (15) (Table S5). In the present study, we obtained similar empirical $\epsilon^{182}\text{W}$ vs. $\epsilon^{196}\text{Pt}$ correlations for the IC and IIIIE groups (Fig. S3), yielding preexposure $\epsilon^{182}\text{W}$ of -3.45 ± 0.12 (95% conf. interval, $n = 5$) for the IC irons and -3.28 ± 0.06 ($n = 5$) for the IIIIE irons. For the IID irons, we previously obtained a preexposure $\epsilon^{182}\text{W}$ of -3.18 ± 0.11 (15, 36). Based on combined Os and W measurements of Carbo a lower preexposure $\epsilon^{182}\text{W}$ of -3.57 ± 0.21 was reported subsequently (56). However, as Carbo is a strongly irradiated iron meteorite, this lower preexposure $\epsilon^{182}\text{W}$ relied on a large extrapolation, resulting in a rather large uncertainty on $\epsilon^{182}\text{W}$. Here we extended the Pt-W isotope dataset of the IID irons, using samples from Bridgewater, N’Kandhla, and Riches. All newly analyzed IID irons have relatively elevated $\epsilon^{182}\text{W}$ coupled with small or negligible $\epsilon^{196}\text{Pt}$ anomalies (Fig. S3). Together, all investigated IID iron meteorites show a well-defined $\epsilon^{182}\text{W}$ – $\epsilon^{196}\text{Pt}$ correlation with a precise preexposure $\epsilon^{182}\text{W}$ of -3.23 ± 0.04 (95% conf. interval, $n = 12$).

As most of the rare iron meteorite groups comprise only a few meteorites, obtaining reliable $\epsilon^{182}\text{W}$ vs. $\epsilon^{196}\text{Pt}$ correlations to constrain their preexposure $\epsilon^{182}\text{W}$ is not always possible. Thus, for the IIC, IIF, and IIIIF groups, for which we analyzed only two or three samples, the measured $\epsilon^{182}\text{W}$ of each sample was corrected individually using its measured $\epsilon^{196}\text{Pt}$ and the mean $\epsilon^{182}\text{W}$ vs. $\epsilon^{196}\text{Pt}$ slope obtained from the other iron meteorite groups. This approach is valid because the $\epsilon^{182}\text{W}$ vs. $\epsilon^{196}\text{Pt}$ slopes of the major iron meteorite groups are indistinguishable from each other (Fig. S4), resulting in a precisely defined mean $\epsilon^{182}\text{W}$ vs. $\epsilon^{196}\text{Pt}$ slope of 1.320 ± 0.055 (95% conf. interval, $n = 7$). Hence,

the preexposure $\epsilon^{182}\text{W}$ of an individual sample can be determined using the following equation:

$$\epsilon^{182}\text{W}_{\text{preexposure}} = \epsilon^{182}\text{W}_{\text{measured}} - \epsilon^{196}\text{Pt}_{\text{measured}} \times (-1.320 \pm 0.055). \quad [\text{S1}]$$

Using this equation, we calculated preexposure $\epsilon^{182}\text{W}$ values for every sample of the iron meteorite groups investigated here, resulting in average preexposure $\epsilon^{182}\text{W}$ values of -3.45 ± 0.04 (95% conf. interval) for the IC irons, -3.20 ± 0.12 for the IIC irons, -3.23 ± 0.03 for the IID irons, -3.21 ± 0.05 for the IIF irons, -3.27 ± 0.04 for the IIIE irons, and -3.24 ± 0.10 for the IIIF irons (Table S5). For the IC, IID, and IIIE groups, these preexposure $\epsilon^{182}\text{W}$ values are in excellent agreement with those obtained using the empirical Pt-W isotope correlations for these groups (Fig. S3), demonstrating that these two correction methods lead to consistent results.

Hf-W Model Ages of Core Formation. The preexposure $\epsilon^{182}\text{W}$ values can be used to calculate Hf-W model ages for each group of iron meteorites. These ages provide the time of a single event of Hf/W fractionation from a reservoir with chondritic $^{180}\text{Hf}/^{184}\text{W}$, which in case of the iron meteorites presumably occurred by metal-silicate separation during core formation. The model age is calculated using the relation

$$\Delta t = -\frac{1}{\lambda} \ln \left[\frac{(\epsilon^{182}\text{W})_{\text{Sample}} - (\epsilon^{182}\text{W})_{\text{Chondrites}}}{(\epsilon^{182}\text{W})_{\text{SSI}} - (\epsilon^{182}\text{W})_{\text{Chondrites}}} \right], \quad [\text{S2}]$$

where $(\epsilon^{182}\text{W})_{\text{Sample}}$ represents the preexposure $\epsilon^{182}\text{W}$ of any iron meteorite group, $\epsilon^{182}\text{W}_{\text{chondrites}}$ is the composition of carbonaceous chondrites (-1.91 ± 0.08) (57), $\epsilon^{182}\text{W}_{\text{SSI}}$ is the Solar System initial of -3.49 ± 0.07 as obtained from CAI (44), and λ is the decay constant of ^{182}Hf of $0.078 \pm 0.002 \text{ My}^{-1}$ (2σ) (58). The distinct preexposure $\epsilon^{182}\text{W}$ values obtained for the iron meteorite groups from this study (IC, IIC, IID, IIF, IIIE, and IIIF) yield a range of Hf-W model ages from ~ 0.3 My to ~ 2.8 My after CAI formation (Table S5), consistent with the range of ages determined previously for the major iron meteorite groups (IIAB, IIIAB, IVA, and IVB) (15). Nevertheless, the CC iron meteorite groups exhibit on average younger Hf-W model ages of ~ 2.2 – 2.8 My after CAI formation than the NC groups (~ 0.3 – 1.8 My).

Thermal Model. To quantify the relationship between the timing of accretion and core formation, we modeled the thermal evolution of bodies internally heated by ^{26}Al decay (15). This model assumes single-stage core formation at a given temperature, but this assumption is not always valid, especially for volatile-depleted, S-poor bodies (15). In such bodies (e.g., IIIF, IVA, and IVB), silicate melt extraction probably preceded the melting of a significant portion of the Fe metal and also removed most of the heat-producing ^{26}Al from the mantle (59). Thus, heating slowed down considerably following silicate melt extraction, making it difficult to reliably estimate the timing of final metal melting and core formation in these volatile-depleted, S-poor bodies. In contrast, in volatile- and S-rich bodies, most of the Fe metal was already molten at the time of silicate melt extraction, meaning that the separation of silicate and metal melts probably occurred at about the same time. Thus, for modeling the thermal evolution of volatile-rich bodies, the effect of ^{26}Al

removal during silicate melt extraction is inconsequential for estimating the relation between time of core formation and time of parent body accretion. For this reason, any difference in accretion time between CC and NC iron meteorite parent bodies is most easily assessed using the most volatile-rich groups (i.e., NC groups IC and IIAB vs. CC groups IIC, IID, and IIF).

The thermal model used here assumes instantaneous accretion and calculates the temperature vs. time relations for an undifferentiated spherical planetary body that is heated by ^{26}Al decay following accretion. The model accounts for heat production by radioactive decay and for heat loss by conduction. The temperatures were evaluated at half the radius (i.e., $r = 20$ km) of the body. We note that, because bodies essentially heat up isothermally (59, 60), evaluating the temperature at a different radius yields identical results. The parameters used for the thermal model are parent body radius $R = 40$ km, thermal conductivity $K = 2.1 \text{ Wm}^{-1}\text{K}^{-1}$ (60), thermal diffusivity $\kappa = 5.0 \times 10^{-7} \text{ m}^2\text{s}^{-1}$, Solar System initial $^{26}\text{Al}/^{27}\text{Al} = 5.25 \times 10^{-5}$, heat production $A = \text{Al concentration} \times (^{26}\text{Al}/^{27}\text{Al}) \text{ Wm}^{-3}$, decay constant of $^{26}\text{Al} = 9.83 \times 10^{-7} \text{ y}^{-1}$ (61), density of planetesimal $\rho = 3.2 \text{ gcm}^{-3}$, emissivity $h = 1.0 \text{ m}^{-1}$, and the assumed ambient temperature $T_0 = 250 \text{ K}$ (60). The largest uncertainty on the modeling results comes from the assumed Al concentration of the bulk parent bodies. Here we assumed an Al concentration of 12 wt %, which is equivalent to the mean Al concentration of CC chondrites (62). Nevertheless, using different Al concentrations (i.e., as low as 8.65 wt % for CI chondrites or as high as 16.8 wt % for CV chondrites) results in inferred accretion ages that are different by only <0.2 My for NC parent bodies and by <0.4 My for CC parent bodies (Fig. 3).

Silicate melt fractions of 40–60% are necessary for an efficient separation of metal and silicate melts (59, 63, 64), and such high-melt fractions would be reached only at temperatures of $\sim 1,600$ K to $\sim 1,700$ K (64). For volatile- (and S-)rich bodies (i.e., IC, IIAB, IIC, IID, and IIF), this temperature is similar to the liquidus temperature of the core (the IIAB core contains ~ 17 wt % S, corresponding to a liquidus temperature of $\sim 1,600$ K), meaning that in these bodies the entire core segregated in a single instant. For the thermal model used here we thus assume that core formation in the volatile-rich iron meteorite parent bodies occurred at $\sim 1,600$ K. However, even if the temperature of core formation was as low as $\sim 1,400$ K—i.e., the silicate solidus and hence the lowest possible core formation temperature—this would yield inferred accretion ages that are within <0.1 My of those obtained when assuming a temperature of 1,600 K.

The modeling results show that the Hf-W model ages for core formation of ~ 0.3 – 0.7 My obtained for some of the NC iron meteorite parent bodies (IC and IIAB) are consistent with very early accretion within less than ~ 0.4 My after Solar System formation (Fig. 3). In contrast, the younger Hf-W ages of the CC iron meteorite groups (IIC, IID, and IIF) indicate that their parent bodies accreted significantly later, at $0.9^{+0.4}_{-0.2}$ My after Solar System formation. Although the accretion ages of volatile-poor iron meteorite parent bodies are more uncertain, the significantly higher $\epsilon^{182}\text{W}$ of volatile-poor CC groups (IIIF and IVB) over the NC groups (IVA) is fully consistent with the difference in accretion ages inferred from the more volatile-rich iron meteorite groups. Thus, we conclude that iron meteorite parent bodies in the NC reservoir accreted within ~ 0.4 My after CAI formation and those in the CC reservoir slightly later, at $0.9^{+0.4}_{-0.2}$ My after CAI formation.

Table S1. Tungsten isotope compositions of terrestrial metal standard NIST129c determined by MC-ICPMS

Standard ID	$\epsilon^{182}\text{W} (6/3)_{\text{meas.}^*} \pm 2 \text{ SE}$	$\epsilon^{182}\text{W} (6/4)_{\text{meas.}^*} \pm 2 \text{ SE}$	$\epsilon^{183}\text{W} (6/4)_{\text{meas.}^*} \pm 2 \text{ SE}$	$\epsilon^{184}\text{W} (6/3)_{\text{meas.}^*} \pm 2 \text{ SE}$
S04	0.07 ± 0.04	0.03 ± 0.04	-0.03 ± 0.04	0.02 ± 0.03
S04	0.04 ± 0.04	-0.01 ± 0.04	-0.04 ± 0.03	0.03 ± 0.02
S04	-0.04 ± 0.04	-0.06 ± 0.04	-0.02 ± 0.03	0.01 ± 0.02
S04	0.00 ± 0.04	0.02 ± 0.04	0.01 ± 0.04	-0.01 ± 0.02
S04	-0.01 ± 0.08	-0.02 ± 0.09	-0.01 ± 0.07	0.00 ± 0.05
S04	-0.04 ± 0.08	-0.02 ± 0.09	0.01 ± 0.08	-0.01 ± 0.05
S04	0.03 ± 0.07	0.08 ± 0.08	0.04 ± 0.06	-0.02 ± 0.04
S04	0.02 ± 0.09	0.05 ± 0.09	0.02 ± 0.07	-0.01 ± 0.05
S04	0.09 ± 0.07	0.06 ± 0.09	-0.02 ± 0.07	0.01 ± 0.05
S04	-0.01 ± 0.08	-0.03 ± 0.08	-0.01 ± 0.07	0.01 ± 0.05
S04	-0.02 ± 0.07	-0.01 ± 0.08	0.01 ± 0.07	-0.01 ± 0.05
S04	0.02 ± 0.07	-0.01 ± 0.08	-0.03 ± 0.06	0.02 ± 0.04
S04	-0.01 ± 0.07	-0.09 ± 0.08	-0.06 ± 0.06	0.04 ± 0.04
S04	0.05 ± 0.07	0.00 ± 0.08	-0.04 ± 0.07	0.03 ± 0.04
S04	0.06 ± 0.07	0.01 ± 0.08	-0.04 ± 0.06	0.03 ± 0.04
S04	-0.03 ± 0.07	0.05 ± 0.08	0.06 ± 0.06	-0.04 ± 0.04
S04	0.02 ± 0.07	0.05 ± 0.09	0.03 ± 0.07	-0.02 ± 0.05
T07	-0.01 ± 0.06	0.02 ± 0.06	0.03 ± 0.06	-0.02 ± 0.04
T07	-0.01 ± 0.06	-0.01 ± 0.07	0.00 ± 0.06	0.00 ± 0.04
T07	0.06 ± 0.06	0.04 ± 0.07	-0.01 ± 0.06	0.01 ± 0.04
T07	0.08 ± 0.07	0.07 ± 0.06	-0.01 ± 0.06	0.01 ± 0.04
T07	0.18 ± 0.06	0.08 ± 0.07	-0.07 ± 0.06	0.05 ± 0.04
Z08	0.04 ± 0.05	0.05 ± 0.06	0.01 ± 0.05	0.00 ± 0.04
Z08	0.08 ± 0.05	-0.05 ± 0.06	-0.09 ± 0.05	0.06 ± 0.03
Z08	0.06 ± 0.05	0.02 ± 0.06	-0.03 ± 0.05	0.02 ± 0.03
Z08	-0.01 ± 0.05	0.00 ± 0.06	0.00 ± 0.05	0.00 ± 0.03
Z08	0.09 ± 0.05	0.08 ± 0.06	-0.01 ± 0.05	0.00 ± 0.03
Z08	0.10 ± 0.05	0.02 ± 0.06	-0.06 ± 0.05	0.04 ± 0.03
Z08	0.03 ± 0.06	0.08 ± 0.05	0.04 ± 0.05	-0.03 ± 0.04
Z08	-0.04 ± 0.05	-0.09 ± 0.06	-0.04 ± 0.05	0.02 ± 0.03
Z08	0.00 ± 0.05	-0.10 ± 0.06	-0.07 ± 0.05	0.05 ± 0.03
AG04	0.01 ± 0.07	0.01 ± 0.07	0.00 ± 0.07	0.00 ± 0.04
AG04	0.07 ± 0.08	0.00 ± 0.07	-0.05 ± 0.07	0.03 ± 0.04
AG04	0.15 ± 0.06	0.06 ± 0.08	-0.07 ± 0.07	0.05 ± 0.04
AG04	0.02 ± 0.07	0.10 ± 0.07	0.06 ± 0.07	-0.04 ± 0.04
AG04	0.00 ± 0.07	0.00 ± 0.07	0.00 ± 0.07	0.00 ± 0.04
SG	0.02 ± 0.05	0.00 ± 0.07	-0.01 ± 0.05	0.01 ± 0.03
SG	0.01 ± 0.05	-0.01 ± 0.07	-0.01 ± 0.05	0.01 ± 0.03
SG	-0.02 ± 0.05	-0.05 ± 0.07	-0.02 ± 0.05	0.01 ± 0.03
SG	-0.05 ± 0.05	0.03 ± 0.08	0.06 ± 0.05	-0.04 ± 0.03
SG	0.02 ± 0.05	0.02 ± 0.07	0.00 ± 0.05	0.00 ± 0.03
BW09	0.02 ± 0.06	-0.07 ± 0.07	-0.07 ± 0.05	0.04 ± 0.03
BW09	0.03 ± 0.06	0.02 ± 0.07	-0.01 ± 0.05	0.00 ± 0.03
BW09	0.10 ± 0.06	0.02 ± 0.08	-0.06 ± 0.05	0.04 ± 0.03
BW09	0.12 ± 0.06	0.02 ± 0.08	-0.07 ± 0.05	0.05 ± 0.03
BW09	0.08 ± 0.08	0.04 ± 0.08	-0.03 ± 0.06	0.02 ± 0.04
CF10	0.15 ± 0.06	-0.03 ± 0.06	-0.13 ± 0.05	0.09 ± 0.03
CF10	0.06 ± 0.06	-0.01 ± 0.07	-0.05 ± 0.06	0.03 ± 0.04
CC10	0.11 ± 0.06	0.04 ± 0.06	-0.05 ± 0.07	0.03 ± 0.04
CC10	-0.02 ± 0.05	0.06 ± 0.06	0.06 ± 0.05	-0.04 ± 0.04
CC10	0.06 ± 0.05	0.07 ± 0.06	0.01 ± 0.06	0.00 ± 0.04
CC10	0.06 ± 0.05	0.02 ± 0.06	-0.03 ± 0.06	0.02 ± 0.04
Mean, <i>n</i> = 53				
±2 SD	0.04 ± 0.11	0.01 ± 0.09	-0.02 ± 0.08	0.01 ± 0.05
±95% conf. limit	0.04 ± 0.01	0.01 ± 0.01	-0.02 ± 0.01	0.01 ± 0.01

Uncertainties represent 2 SE obtained from within-run statistics.

*Internally normalized to $^{186}\text{W}/^{183}\text{W} = 1.98594$ or to $^{186}\text{W}/^{184}\text{W} = 0.92767$.

Table S2. Platinum isotope compositions of metal samples determined by MC-ICPMS

Sample Group	Collection, no.	N	Normalized to $^{196}\text{Pt}/^{195}\text{Pt}$			Normalized to $^{198}\text{Pt}/^{195}\text{Pt}$		
			$\epsilon^{192}\text{Pt}, \pm 2 \text{ SD}$	$\epsilon^{194}\text{Pt}, \pm 2 \text{ SD}$	$\epsilon^{198}\text{Pt}, \pm 2 \text{ SD}$	$\epsilon^{192}\text{Pt}, \pm 2 \text{ SD}$	$\epsilon^{194}\text{Pt}, \pm 2 \text{ SD}$	$\epsilon^{196}\text{Pt}, \pm 2 \text{ SD}$
IC iron meteorites								
Chihuahua City	BM 1959, 1011	1	0.76 ± 1.30	0.24 ± 0.13	-0.20 ± 0.22	0.50 ± 1.30	0.17 ± 0.11	0.07 ± 0.07
Murnpeowie	BM 2005, M179	2	5.11 ± 1.30	0.88 ± 0.13	-1.15 ± 0.22	3.95 ± 1.30	0.50 ± 0.11	0.38 ± 0.07
Murnpeowie (replicate)	BM 2005, M179	4	3.11 ± 1.02	0.55 ± 0.14	-0.76 ± 0.16	2.34 ± 1.05	0.29 ± 0.11	0.26 ± 0.05
Arispe	Münster	6	14.30 ± 0.29	0.84 ± 0.04	-1.04 ± 0.09	13.33 ± 0.27	0.52 ± 0.03	0.35 ± 0.03
Arispe (replicate)	Münster	6	13.81 ± 0.22	0.80 ± 0.06	-1.03 ± 0.12	12.89 ± 0.36	0.48 ± 0.04	0.32 ± 0.04
Bendego	USNM #351	2	1.01 ± 1.30	0.90 ± 0.13	-1.55 ± 0.22	-0.57 ± 1.30	0.38 ± 0.11	0.52 ± 0.07
Arispe	ME 1011	3	14.97 ± 1.30	1.08 ± 0.13	-1.25 ± 0.22	13.69 ± 1.30	0.67 ± 0.11	0.42 ± 0.07
Bendego	ME 6	3	2.52 ± 1.30	0.80 ± 0.13	-1.42 ± 0.22	1.08 ± 1.30	0.32 ± 0.11	0.47 ± 0.07
IIC iron meteorites								
Kumerina	BM 1938, 220	2	0.94 ± 1.30	0.21 ± 0.13	-0.13 ± 0.22	0.80 ± 1.30	0.17 ± 0.11	0.04 ± 0.07
Kumerina (replicate)	BM 1938, 220	3	-0.08 ± 1.30	0.01 ± 0.13	0.07 ± 0.22	-0.02 ± 1.30	0.04 ± 0.11	-0.02 ± 0.07
Wiley	BM 1959, 914	4	0.69 ± 1.12	0.15 ± 0.01	-0.14 ± 0.21	0.55 ± 1.34	0.12 ± 0.05	0.05 ± 0.07
Wiley (replicate)	BM 1959, 914	5	0.81 ± 0.65	0.19 ± 0.09	-0.25 ± 0.18	0.58 ± 0.65	0.11 ± 0.06	0.08 ± 0.06
Ballinoo	ME 980	3	-0.44 ± 1.30	0.06 ± 0.13	0.04 ± 0.22	-0.37 ± 1.30	0.08 ± 0.11	-0.01 ± 0.07
IID iron meteorites								
Bridgewater	ME 1895	5	0.70 ± 0.90	0.00 ± 0.09	0.04 ± 0.05	0.80 ± 0.90	0.02 ± 0.08	-0.01 ± 0.02
N'Kandhla	BM 1921, 17	5	0.65 ± 0.29	0.03 ± 0.09	-0.03 ± 0.16	0.64 ± 0.23	0.03 ± 0.05	0.01 ± 0.05
Richa	BM 1966, 55	4	1.28 ± 0.26	-0.01 ± 0.05	0.06 ± 0.11	1.36 ± 0.30	0.01 ± 0.07	-0.02 ± 0.04
IIF iron meteorites								
Monahans	BM 1959, 910	4	1.10 ± 0.87	0.22 ± 0.07	-0.21 ± 0.12	0.91 ± 0.90	0.15 ± 0.05	0.07 ± 0.04
Monahans (replicate)	BM 1959, 910	2	1.67 ± 1.30	0.17 ± 0.13	-0.23 ± 0.22	1.43 ± 1.30	0.09 ± 0.11	0.08 ± 0.07
IIIE iron meteorites								
Willow Creek	Münster	1	0.95 ± 1.30	0.27 ± 0.13	-0.40 ± 0.22	0.55 ± 1.30	0.14 ± 0.11	0.13 ± 0.07
Kokstad	ME 1015	1	2.74 ± 1.30	0.74 ± 0.13	-1.05 ± 0.22	1.62 ± 1.30	0.38 ± 0.11	0.35 ± 0.07
Kokstad (replicate)	ME 1015	2	1.62 ± 1.30	0.57 ± 0.13	-0.77 ± 0.22	0.82 ± 1.30	0.29 ± 0.11	0.26 ± 0.07
Colonia Obrera	ME 2871	1	0.14 ± 1.30	0.07 ± 0.13	0.03 ± 0.22	0.17 ± 1.30	0.06 ± 0.11	-0.01 ± 0.07
Colonia Obrera (replicate)	ME 2871	1	-0.17 ± 1.30	0.10 ± 0.13	-0.09 ± 0.22	-0.30 ± 1.30	0.08 ± 0.11	0.03 ± 0.07
Staunton	BM 1955, M239	1	-0.10 ± 1.30	0.17 ± 0.13	0.22 ± 0.22	-0.17 ± 1.30	0.15 ± 0.11	-0.07 ± 0.07
Staunton (replicate)	BM 1955, M239	2	-0.16 ± 1.30	0.14 ± 0.13	-0.16 ± 0.22	-0.28 ± 1.30	0.08 ± 0.11	0.05 ± 0.07
Paneth's Iron	BM 2005, M199	2	0.55 ± 1.30	0.19 ± 0.13	-0.26 ± 0.22	0.26 ± 1.30	0.12 ± 0.11	0.09 ± 0.07
IIIF iron meteorites								
Klamath Falls	ME 2789	1	0.98 ± 1.30	0.09 ± 0.13	-0.18 ± 0.22	0.39 ± 1.30	0.06 ± 0.11	0.06 ± 0.07
Klamath Falls (replicate)	ME 2789	1	0.97 ± 1.30	0.12 ± 0.13	0.02 ± 0.22	0.99 ± 1.30	0.13 ± 0.11	-0.01 ± 0.07
Clark County	BM 1959, 949	4	2.88 ± 0.99	0.11 ± 0.11	-0.08 ± 0.22	2.81 ± 0.78	0.08 ± 0.06	0.03 ± 0.07
Clark County (replicate)	BM 1959, 949	2	3.79 ± 1.30	0.27 ± 0.13	-0.29 ± 0.22	3.54 ± 1.30	0.17 ± 0.11	0.10 ± 0.07
Terrestrial metal standard								
NIST129c #1		2	0.51 ± 1.30	0.10 ± 0.13	-0.15 ± 0.22	0.38 ± 1.30	0.08 ± 0.11	0.05 ± 0.07
NIST129c #2		7	0.66 ± 0.24	0.07 ± 0.10	-0.07 ± 0.10	0.58 ± 0.25	0.04 ± 0.07	0.02 ± 0.03
NIST129c #3		1	0.36 ± 1.30	0.02 ± 0.13	-0.08 ± 0.22	0.28 ± 1.30	-0.01 ± 0.11	0.03 ± 0.07
NIST129c #4		4	0.99 ± 1.23	0.04 ± 0.11	0.02 ± 0.15	0.97 ± 1.31	0.04 ± 0.08	-0.01 ± 0.05

Instrumental mass fractionation was corrected using the exponential law by internal normalization to $^{198}\text{Pt}/^{195}\text{Pt} = 0.2145$ or to $^{196}\text{Pt}/^{195}\text{Pt} = 0.7464$. *N*, number of solution replicates. The uncertainties reported for $\epsilon^i\text{Pt}$ values of samples, in the case $n < 4$, represent the 2 SD ($n = 63$) obtained from repeated analyses of the terrestrial standard NIST129c (15): [± 1.3 for $\epsilon^{192}\text{Pt}$ (6/5), ± 0.13 for $\epsilon^{194}\text{Pt}$ (6/5), ± 0.22 for $\epsilon^{198}\text{Pt}$ (6/5), ± 1.3 for $\epsilon^{192}\text{Pt}$ (8/5), ± 0.11 for $\epsilon^{194}\text{Pt}$ (8/5), ± 0.07 for $\epsilon^{196}\text{Pt}$ (8/5)] or in the case $n > 4$, the 95% conf. limits of the mean [i.e., according to $(\text{SD} \times t_{0.95, N-1})/\sqrt{N}$].

Table S4. Molybdenum isotope compositions of iron meteorites analyzed by MC-ICPMS

Meteorite Group	Collection, no.	ID	<i>N</i>	$\epsilon^{92}\text{Mo}, \pm 95\%$ conf.	$\epsilon^{94}\text{Mo}, \pm 95\%$ conf.	$\epsilon^{95}\text{Mo}, \pm 95\%$ conf.	$\epsilon^{97}\text{Mo}, \pm 95\%$ conf.	$\epsilon^{100}\text{Mo}, \pm 95\%$ conf.
IC iron meteorites								
Chihuahua City	BM 1959, 1011	BW01	8	0.96 ± 0.12	0.86 ± 0.08	0.34 ± 0.07	0.20 ± 0.08	0.27 ± 0.13
Murnpeowie	BM 2005, M179	BW02	8	1.16 ± 0.20	1.11 ± 0.20	0.41 ± 0.05	0.27 ± 0.05	0.37 ± 0.08
IIC iron meteorites								
Kumerina	BM 1938, 220	BW03	8	2.91 ± 0.28	2.34 ± 0.18	1.50 ± 0.08	0.79 ± 0.10	0.92 ± 0.09
Wiley	BM 1959, 914	BW04	8	4.14 ± 0.22	3.39 ± 0.13	2.19 ± 0.11	1.19 ± 0.11	1.54 ± 0.14
Ballinoo	ME 980	CJ01	8	2.76 ± 0.13	2.19 ± 0.10	1.60 ± 0.09	0.89 ± 0.09	1.01 ± 0.10
IID iron meteorites								
Bridgewater	ME 1895	BT02	7	1.63 ± 0.10	1.16 ± 0.16	0.96 ± 0.15	0.51 ± 0.12	0.67 ± 0.17
IIF iron meteorites								
Monahans	BM 1959, 910	CC01	8	1.50 ± 0.21	1.11 ± 0.13	0.94 ± 0.08	0.50 ± 0.08	0.63 ± 0.13
IIIE iron meteorites								
Kokstad	ME 1015	BW05	8	0.98 ± 0.17	0.86 ± 0.14	0.33 ± 0.13	0.26 ± 0.09	0.28 ± 0.08
Colonia Obreira	ME 2871	BW06	8	1.03 ± 1.36	0.97 ± 0.16	0.35 ± 0.09	0.25 ± 0.14	0.35 ± 0.12
Staunton	BM 1955, M239	BW07	8	1.02 ± 0.16	0.95 ± 0.10	0.41 ± 0.11	0.30 ± 0.08	0.39 ± 0.11
Paneth's iron	BM 2005, M199	BW08	8	1.09 ± 0.15	0.93 ± 0.20	0.42 ± 0.07	0.35 ± 0.05	0.37 ± 0.12
IIIF iron meteorites								
Klamath Falls	ME 2789	CC02	8	1.70 ± 0.18	1.20 ± 0.18	0.98 ± 0.06	0.56 ± 0.11	0.62 ± 0.09
Clark County	BM 1959, 949	CC03	6	1.45 ± 0.23	1.20 ± 0.17	1.00 ± 0.06	0.54 ± 0.04	0.59 ± 0.23

Instrumental mass bias was corrected using the exponential law by internal normalization to $^{98}\text{Mo}/^{96}\text{Mo} = 1.453173$. *N*, number of solution replicates. The uncertainties reported for measured $\epsilon^i\text{Mo}$ values of samples (subscript "meas.") represent the 95% conf. limits of the mean [i.e., according to $(SD \times t_{0.95, N-1})/\sqrt{N}$].

Table S5. Preexposure $\epsilon^{182}\text{W}$, $\epsilon^{183}\text{W}$, and Hf-W model ages of iron meteorite groups

Iron Meteorite Group	<i>N</i>	$\epsilon^{182}\text{W}_{\text{preexposure}}, 95\%$ conf.	$\epsilon^{183}\text{W}, \pm 95\%$ conf.	$\Delta t_{\text{CAI}}^*, \text{My}, \pm 2\sigma$
NC reservoir				
IC	5	-3.45 ± 0.04	-0.05 ± 0.02	0.3 ± 0.5
IIAB	8	-3.40 ± 0.03	-0.02 ± 0.02	0.8 ± 0.5
IIIAB	13	-3.35 ± 0.03	-0.03 ± 0.02	1.2 ± 0.5
IIIE	5	-3.28 ± 0.06	-0.05 ± 0.04	1.8 ± 0.7
IVA	6	-3.32 ± 0.05	0.00 ± 0.07	1.5 ± 0.6
CC reservoir				
IIC	2	-3.20 ± 0.12	0.30 ± 0.04	2.6 ± 1.3
Wiley (IIC)	1	-3.23 ± 0.11	0.52 ± 0.06	2.3 ± 1.2
IID	12	-3.23 ± 0.04	0.13 ± 0.01	2.3 ± 0.6
IIF	1	-3.21 ± 0.05	0.09 ± 0.02	2.5 ± 0.7
IIIF	2	-3.24 ± 0.10	0.08 ± 0.07	2.2 ± 1.1
IVB	14	-3.18 ± 0.05	0.13 ± 0.02	2.8 ± 0.7

*Two-stage Hf-W model age of core formation (in million years), given relative to the time of CAI formation.